Title

Hyperpolarized [2—13C]pyruvate MR molecular imaging with whole brain coverage

Authors

Chung, Brian T
Kim, Yaewon
Gordon, Jeremy W
et al.

Publication Date

2023-10-01

DOI

10.1016/j.neuroimage.2023.120350

Peer reviewed

Published in final edited form as:

Neuroimage. 2023 October 15; 280: 120350. doi:10.1016/j.neuroimage.2023.120350.

Hyperpolarized [2–^{13}C]pyruvate MR molecular imaging with whole brain coverage

Brian T. Chung[a,b,1], **Yaewon Kim**[a,1,*], **Jeremy W. Gordon**[a], **Hsin-Yu Chen**[a], **Adam W. Autry**[a], **Philip M. Lee**[a,b], **Jasmine Y. Hu**[a,b], **Chou T. Tan**[c], **Chris Suszczynski**[c], **Susan M. Chang**[d], **Javier E. Villanueva-Meyer**[a], **Robert A. Bok**[a], **Peder E.Z. Larson**[a,b], **Duan Xu**[a,b], **Yan Li**[a], **Daniel B. Vigneron**[a,b,d]

[a]Department of Radiology and Biomedical Imaging, University of California, 1700 Fourth Street, Byers Hall Suite 102, San Francisco, CA 94158, USA

[b]UCSF – UC Berkeley Graduate Program in Bioengineering, University of California, USA

[c]ISOTEC Stable Isotope Division, MilliporeSigma, Merck KGaA, Miamisburg, OH 45342, USA

[d]Department of Neurological Surgery, University of California, San Francisco, CA 94158, USA

Abstract

Hyperpolarized (HP) ^{13}C Magnetic Resonance Imaging (MRI) was applied for the first time to image and quantify the uptake and metabolism of [2–^{13}C]pyruvate in the human brain to provide new metabolic information on cerebral energy metabolism. HP [2–^{13}C]pyruvate was injected intravenously and imaged in 5 healthy human volunteer exams with whole brain coverage in a 1-minute acquisition using a specialized spectral-spatial multi-slice echoplanar imaging (EPI) pulse sequence to acquire ^{13}C-labeled volumetric and dynamic images of [2–^{13}C] pyruvate and downstream metabolites [5–^{13}C]glutamate and [2–^{13}C]lactate. Metabolic ratios and apparent conversion rates of pyruvate-to-lactate (k_{PL}) and pyruvate-to-glutamate (k_{PG}) were quantified to investigate simultaneously glycolytic and oxidative metabolism in a single injection.

Keywords

Hyperpolarized carbon-13; Molecular imaging; Brain Metabolism

*Corresponding author. yaewon.kim@ucsf.edu (Y. Kim).
[1]These authors contributed equally to this work.

CRediT authorship contribution statement

Brian T. Chung: Conceptualization, Formal analysis, Methodology, Investigation, Writing – original draft. **Yaewon Kim:** Formal analysis, Methodology, Visualization, Writing – review & editing. **Jeremy W. Gordon:** Conceptualization, Methodology, Writing – review & editing. **Hsin-Yu Chen:** Methodology, Writing – review & editing. **Adam W. Autry:** Methodology, Writing – review & editing. **Philip M. Lee:** Writing – review & editing. **Jasmine Y. Hu:** Writing – review & editing. **Chou T. Tan:** Methodology, Writing – review & editing. **Chris Suszczynski:** Methodology, Writing – review & editing. **Susan M. Chang:** Conceptualization, Funding acquisition, Writing – review & editing. **Javier E. Villanueva-Meyer:** Conceptualization, Writing – review & editing. **Robert A. Bok:** Conceptualization, Methodology, Writing – review & editing. **Peder E.Z. Larson:** Conceptualization, Methodology, Writing – review & editing. **Duan Xu:** Conceptualization, Funding acquisition, Writing – review & editing. **Yan Li:** Conceptualization, Funding acquisition. **Daniel B. Vigneron:** Conceptualization, Methodology, Funding acquisition, Supervision, Writing – review & editing.

Supplementary materials

Supplementary material associated with this article can be found, in the online version, at doi:10.1016/j.neuroimage.2023.120350.

1. Introduction

Hyperpolarized (HP) carbon-13 MR using dissolution Dynamic Nuclear Polarization (dDNP) has been investigated in animals since 2006 to provide a unique window into cellular metabolism, enabling the quantification of enzyme-catalyzed conversion rates that inform on critical cellular biochemistry in both normal and pathologic conditions as well as perfusion information (Ardenkjaer-Larsen et al., 2003; Golman et al., 2003; Golman et al., 2006; Kurhanewicz et al., 2019). A first-in-human proof-of-concept clinical trial of HP [1–^{13}C]pyruvate completed in 2013 demonstrated feasibility and safety in patients (Nelson et al., 2013). The subsequent development of commercial research polarizers enabled new technical developments and initial human studies over the past 5 years in a variety of applications including prostate cancer, brain tumors, renal cancer, cardiac disease, pancreatic cancer, traumatic brain injury and breast cancer (Granlund et al., 2020; Miloushev et al., 2018; Cunningham et al., 2016; Abeyakoon et al., 2019; Gallagher et al., 2020; Stødkilde-Jørgensen et al., 2020; Tran et al., 2019; Aggarwal et al., 2017; Park et al., 2018; Autry et al., 2019; Grist et al., 2019; Autry et al., 2020; Gordon et al., 2020; Hackett et al., 2020; Autry et al., 2021; Kim et al., 2021; Li et al., 2021; Chen et al., 2021). Since 2018, studies have investigated cerebral energy metabolism with HP [1–^{13}C]pyruvate in the normal brain and neuro-pathologies, demonstrating novel insights into brain bioenergetics by measuring the conversion of pyruvate to lactate catalyzed by the enzyme lactate dehydrogenase (LDH) and pyruvate to bicarbonate via pyruvate dehydrogenase (PDH) (Miloushev et al., 2018; Park et al., 2018; Autry et al., 2019; Grist et al., 2019; Autry et al., 2020; Gordon et al., 2020; Hackett et al., 2020; Autry et al., 2021; Kim et al., 2021; Li et al., 2021; Chen et al., 2021).

While HP [1–^{13}C]pyruvate has successfully been utilized as a probe in over 500 patient studies to quantify the conversion to [1–^{13}C]lactate and [^{13}C]bicarbonate in the human brain, its metabolism and conversion to $^{13}CO_2$ through PDH prevents direct detection of TCA cycle metabolism (Li et al., 2021). To address this, we investigated HP ^{13}C-pyruvate labeled in the C2 position to provide a unique MR molecular imaging window into the TCA cycle as the labeled carbon is carried over to acetyl-CoA and enables the observation of [5–^{13}C] glutamate after enzyme catalyzed conversion from α-ketoglutarate (Chung et al., 2019). In the human brain, glutamate is the most abundant free amino acid and is at a crossroad between multiple metabolic pathways (Petroff, 2002; Segovia et al., 2001). Glutamate plays a significant role as an excitatory neurotransmitter that is critical for neuronal signal transmission in the brain and throughout the nerves in the body and plays an important role during brain development while shaping learning and memory (Petroff, 2002). Glutamate has also been shown to decrease in aging and neurodegeneration, and *in vivo* MR spectroscopy studies exploring changes in neurometabolite concentrations in patients with grade 2 & 3 IDH-mutant gliomas detected reduced levels of glutamate (Segovia et al., 2001; Hoerst et al., 2010; Autry et al., 2022). Studies have also shown that conversion of α-ketoglutarate to glutamate is reduced in isocitrate dehydrogenase 1 (IDH1) mutant cells and brain tumor models providing additional information on IDH1 metabolic reprogramming (Chaumeil et al., 2014).

In order to investigate [2–^{13}C]pyruvate metabolism in the brain, we developed the required methods for the production of sterile HP doses of GMP [2–^{13}C]pyruvate (Chung et al., 2019). Our initial first-in-human study using non-localized HP ^{13}C MR spectroscopy demonstrated the feasibility of obtaining human HP [2–^{13}C]pyruvate brain data, but did not provide the ability to image metabolic conversions throughout the brain as is required for detection of both normal and pathologic variations (Chung et al., 2019). While [2–^{13}C]pyruvate has the potential to provide direct information about TCA cycle metabolism, there are significant challenges in imaging its metabolic conversion due to its broad chemical shift dispersion, and lactate signals have a shorter T_1 and peak-splitting due to J_{CH} coupling. Recent technical advances, including variable-resolution echo-planar imaging (EPI) (Gordon et al., 2020) and patch-based higher order singular value decomposition (HOSVD) (Kim et al., 2021), have enabled higher spatial resolution and improved image quality in HP ^{13}C MRI. In this project, we developed a multi-slice, dynamic HP [2–^{13}C]pyruvate EPI pulse sequence and incorporated spatiotemporal patch-based denoising methods to apply this technique for the first time in healthy volunteer studies with whole brain coverage to investigate its application for monitoring cerebral energy metabolism using HP [2–^{13}C]pyruvate.

2. Material and methods

2.1. [2–^{13}C]pyruvate preparation

Hyperpolarization was performed using a 5T SPINlab dDNP polarizer (GE Healthcare) operating at 0.8 K. Samples containing 1.47 g [2–^{13}C] pyruvic acid (ISOTEC Stable Isotope Division, MilliporeSigma, Merck KGaA) and 15 mM electron paramagnetic agent (AH111501, GE Healthcare) were prepared the morning of the study and polarized for at least two hours. Samples were then rapidly dissolved using superheated water and the electron paramagnetic agent was removed by filtration prior to neutralization with a TRIS-buffered NaOH solution. Prior to injection, the pH, pyruvate and residual EPA concentrations, polarization, and sample temperature were rapidly measured with an integrated quality control (QC) module. In parallel, the integrity of the 0.2 μm sterile filter was tested in agreement with manufacturer specifications prior to injection. After release by the pharmacist, a 0.43 mL/kg dose of 241 ± 7 mM pyruvate (n = 5) was injected at a rate of 5 mL/s, followed by a 20 mL sterile saline flush (0.9% sodium chloride, Baxter Healthcare Corporation). The liquid-state polarization was 28.2 ± 6.8%, and the average time elapsed between the start of dissolution and the start of IV injection was 48.8 ± 1.9 s.

2.2. Human MR imaging protocol: [2–^{13}C]pyruvate spectral-spatial pulse with EPI

Imaging studies were performed on a 3T clinical MR system (MR750, GE Healthcare, Waukesha, WI) using a commercially available 8-channel ^{1}H / 24-channel ^{13}C head coil (RAPID Biomedical, Germany) with an integrated ^{13}C birdcage volume exciter for RF transmit. The ^{13}C RF power was calibrated using a head phantom containing natural abundance ethylene glycol prior to the study. All ^{13}C MR data was acquired with a variable resolution, metabolite-selective EPI pulse sequence (Gordon et al., 2020). Using an RF toolbox (https://github.com/LarsonLab/hyperpolarized-mri-toolbox), the singleband spectral-spatial (SPSP) RF pulse was designed to independently excite [2–^{13}C]pyruvate,

[5–^{13}C]glutamate, and downfield and upfield resonances of [2–^{13}C]lactate with minimal off-resonance excitation (Fig. 1 and Supplementary Fig. 1). To avoid J-coupling artifacts, the downfield and upfield peaks of [2–^{13}C]lactate were acquired independently. Using a multi-resolution approach, [2–^{13}C]pyruvate was acquired with in-plane spatial resolution of 7.5 × 7.5 mm^2 and 20° tip angle, while the downstream metabolites [5–^{13}C]glutamate and the [2–^{13}C]lactate doublet were acquired with an in-plane resolution of 22.5 × 22.5 mm^2 and 60° tip angle. Five 3-cm slices were acquired with a matrix size of 32×32. 20 timeframes were acquired per metabolite with 3 s temporal resolution (TR) for a total scan time of 60 s. T_1 -weighted ^{1}H IR-SPGR (inversion recovery - spoiled gradient recalled) images and T_2-weighted ^{1}H FLAIR (fluid-attenuated inversion recovery) were acquired for anatomical reference. Four healthy volunteers were imaged following IRB and FDA-IND approved protocols with informed consent. Persons ranging in age from 29 to 60 years old were imaged at approximately midday with one volunteer scanned twice on different days yielding a total of 5 datasets.

2.3. Data analysis and quantitative post-processing

Following k-space noise pre-whitening, optimal coil combination techniques were performed across multichannel datasets with [2–^{13}C] pyruvate end of scan timeframes serving as signalless floors to determine noise covariance (Kim et al., 2021; Zhu et al., 2019). Image reconstruction was performed using the Orchestra toolbox (GE Healthcare) in MATLAB. The HP ^{13}C data was phased and denoised using a patch-based higher order singular value decomposition (HOSVD) method (Kim et al., 2021; Vaziri et al., 2022). In this study the following parameters were used in denoising all cases: kglobal = 0.4; klocal = 0.8 (scales used to determine thresholds); step = 2. In low-resolution cases: patch size = 3; radius of search window size = 4; and in high-resolution cases: patch size = 5; radius of search window size = 6. These parameters were chosen based on the optimal values found from the ^{13}C MR EPI images of the human brain with HP [1–^{13}C]pyruvate MRI (Kim et al., 2021). Signal maps for each metabolite were generated by normalizing voxels to global peak pyruvate signal. In the case of lactate, the upfield and downfield signals were individually processed and combined to yield a total lactate image. To assess image similarity between the upfield and downfield lactate images, structural similarity index measure (SSIM (Zhou et al., 2004)) was calculated using MATLAB. Area-Under-Curve (AUC) images for each metabolite were composed by summing data through time. From the AUC images, ratios of [5–^{13}C]glutamate-to-[2–^{13}C]pyruvate, [2–^{13}C]lactate-to-[2–^{13}C]pyruvate, and [5–^{13}C]glutamate-to-[2–^{13}C]lactate were calculated. Voxel-wise calculations for pyruvate-to-glutamate conversion rate (k_{PG}) and pyruvate-to-lactate conversion rate (k_{PL}) were performed using an irreversible, three-site exchange kinetic model (Larson et al., 2018). In the kinetic fitting, B_1 field strength was scaled to 80%, and T_1 relaxation time constants were chosen to optimally fit data. Analytical tools used for the kinetic fitting are available from the Hyperpolarized MRI Toolbox (https://github.com/LarsonLab/hyperpolarized-mri-toolbox). A brain mask for HP ^{13}C data was created from T_1- and T_2-weighted images utilizing the FLIRT and FSL FAST algorithms for ^{1}H image alignment and white matter segmentation (Jenkinson and Smith, 2001; Zhang et al., 2001). For kinetic analyses, a brain mask was created again with ^{13}C brain voxels containing > 40% of white matter and gray matter and applied to the resulting AUC ratio

and kinetic rate maps. When evaluating the average k_{PL}, k_{PG}, and AUC ratios for the whole brain, only the voxels with SNR of the AUC data (SNR_{AUC}) greater than 3 for each metabolite were used, and those with fitting error less than 30% were used for calculating the average kinetic rates.

3. Results

3.1. Hyperpolarized [2–^{13}C]pyruvate MR imaging

Fig. 2 shows denoised dynamic images of HP [2–^{13}C]pyruvate, [5–^{13}C]glutamate, and upfield and downfield [2–^{13}C]lactate in the brain of a healthy volunteer. The dynamic upfield and downfield lactate images are free of ghosting or blurring that could have been attributed to J-coupling. Quantitatively, close agreement was observed between the upfield and downfield lactate images with high correlation ($r = 0.97$, Supplementary Figure 2) and a structural similarity index measure (SSIM (Zhou et al., 2004)) of 0.91 in this subject. Across all studies, r values of 0.85 ± 0.10 and SSIM of 0.88 ± 0.02 were obtained.

Fig. 3 shows AUC images from the same volunteer overlaid on ^{1}H IR-SPGR images. Signal intensity of lactate and glutamate was normalized to the pyruvate signal. High resolution pyruvate data acquired at 0.75×0.75 cm^2 shows strong arterial and venous signal well separated from surrounding tissue. Coarser resolution glutamate and lactate data acquired at 2.25×2.25 cm^2 achieved sufficiently high SNR of whole brain coverage. With image denoising, the maximum SNR was 1147 for pyruvate, 65 for glutamate, and 278 and 275 for downfield and upfield lactate signals, respectively, which were 5.6-fold higher for pyruvate, 3.7 for glutamate, and 5.5 for downfield and 6.5 for upfield lactate relative to the raw SNR in this volunteer. The comparison of pre- and post-denoised images are displayed in Supplementary Figure 3. The mean SNR gain from all 5 studies was 7.1 ± 1.0 for pyruvate and 4.5 ± 0.5 for glutamate, 5.4 ± 1.2 for downfield and 5.1 ± 1.0 for upfield lactate.

Top row images in Fig. 4 show ^{13}C AUC images of pyruvate, glutamate, and summed lactate (downfield and upfield) from a separate volunteer. The sagittal image depicts the anatomical position calculated from the DICOM header of the acquired slice. Adjacent signal overlays show similar distributions of [2–^{13}C]pyruvate and downstream metabolites of [2–^{13}C]lactate and [5–^{13}C]glutamate as those observed in the volunteer data above (Vol-1). Also, both lactate and glutamate signals are high in cerebral cortex but low in white matter while signals in the left posterior of the brain can be seen higher than the contralateral side.

3.2. Kinetic rates (k_{PG}, k_{PL}) and metabolite AUC ratios

From the dynamic images of pyruvate, lactate, and glutamate signals, kinetic rates and metabolite AUC ratios can be determined. For example, middle-row plots in Fig. 4 present traces of pyruvate and its metabolite signals from selected voxels in three disparate regions and the kinetic fits determined for lactate and glutamate. Each selected voxel dynamics in the middle row showed k_{PL} values of 0.0084, 0.012, and 0.0071 s^{-1} and k_{PG} values of 0.0011, 0.0019, and 0.0010 s^{-1}, respectively. The representative k_{PL} and k_{PG} maps obtained from healthy volunteer brain data are shown overlaid on the relevant axial T_1-weighted image (bottom row images in Fig. 4). The average of voxelwise k_{PL} and k_{PG}

values from five datasets were determined to be 0.0096 ± 0.0008 s^{-1} and 0.0014 ± 0.0001 s^{-1} which was a magnitude of order lower than k_{PL}. The number of voxels comprising the k_{PL} maps increased by 1.2 to 3.1 times with denoising as more voxels with k_{PL} fulfilled the SNR and fitting error criteria, resulting in covering 89 to 99% of the brain voxels. Likewise, the k_{PG} coverage was increased by 2 to 7 times after denoising. AUC ratios of Σ[2–^{13}C]lactate-to-[2–^{13}C]pyruvate, [5–^{13}C]glutamate-to-[2–^{13}C]pyruvate, and [5–^{13}C]glutamate-to-Σ[2–^{13}C]lactate were calculated voxel-by-voxel from the five volunteer datasets, and the mean (± S.E.) values were 0.26 ± 0.02, 0.037 ± 0.004, and 0.14 ± 0.01, respectively.

4. Discussion

In this project, multi-slice, dynamic HP [2–^{13}C]pyruvate EPI was developed and applied in healthy volunteer studies for the first time to investigate its in-vivo application for human brain research. A variable resolution multi-slice EPI approach to achieve whole brain coverage was utilized enabling the acquisition of glutamate images and a quantification of spatial and temporal distribution for future studies and pathology (Gordon et al., 2020). The observed spatial distributions of [2–^{13}C] lactate and [5–^{13}C]glutamate were consistent with previous studies on the lactate and bicarbonate (indirect measure of a flux to oxidative metabolism) distributions from HP [1–^{13}C]pyruvate MRI (Lee et al., 2020) and the glutamate map from steady-state ^{1}H MRSI (Bogner et al., 2012; Hangel et al., 2021) in the normal human brain. However, in brain tumors, it is expected that [2–^{13}C]lactate signal would be high and ^{13}C-glutamate signal would be low in lesions due to reduced oxidative energy metabolism, similar to the results from a [1–^{13}C]pyruvate brain tumor study that demonstrated the lactate signal was elevated in the tumors while a pyruvate-to-bicarbonate conversion rate (k_{PB}) was greatly reduced compared to normative brain (Park et al., 2018). We observed a slight asymmetry of metabolite signals in the left and right hemisphere, which may be caused by inhomogeneous coil sensitivity or perhaps there is actually an asymmetry in the metabolites. To correct for RF inhomogeneity, applying an intensity correction method such as using ^{23}Na sensitivity profile (Sanchez-Heredia et al., 2022), a numerical model with known coil location and dimensions (Dominguez-Viqueira et al., 2016), and bias correction method (Lu et al., 2022) can be considered.

Due to a lower ^{13}C polarization and faster T_1 relaxation of [2–^{13}C] pyruvate (T_1 = 47 s (Chung et al., 2019)), we used a coarser spatial resolution for lactate and glutamate than those typically used in [1–^{13}C] pyruvate MRI studies of the human brain. A patch-based higher-order singular value decomposition (HOSVD) denoising method was applied to datasets to further improved visualization of the metabolite signals and quantification of k_{PL} and k_{PG} kinetic conversion rates (Kim et al., 2021). With denoising, the number of voxels with k_{PL} fulfilling the SNR and fitting error criteria increased by approximately 3-fold, resulting in 89 to 99% brain coverage, and the k_{PG} coverage was increased by 2- to 7-fold depending on the SNR of the original data. While low SNR in the raw data can bias quantification, error in the estimated rate constants is expected to be less than 20% when the original $SNR_{AUC} \geq 3$ (Kim et al., 2021). Other methods to improve image quality, including deuteration of the dissolution media as well as substrate (Keshari and Wilson, 2014) could

preserve polarization and help improve SNR and consequently spatial resolution to better characterize cerebral metabolism.

We observed an average k_{PG}-to-k_{PL} ratio of ~1/7, which is smaller than the ~1/3 to ~1/6 k_{PB}-to-k_{PL} ratio observed with HP [1–^{13}C]pyruvate (Kim et al., 2021; Grist et al., 2019). These relative values are in agreement with the underlying biochemistry, as conversion of pyruvate-to-bicarbonate by PDH occurs before conversion to glutamate as a byproduct of the TCA cycle and are both quantified by a single unidirectional rate constant. A unidirectional kinetic model was used to determine the kinetic rates since it has been shown to be a simple and robust approach to quantify metabolic conversion of hyperpolarized substrates (Larson et al., 2018; Sun et al., 2018; Mammoli et al., 2020). However, recent studies using HP [1–^{13}C]-pyruvate MRI study have provided further evidence that astrocyte-neuron lactate shuttling contributes to the [1–^{13}C]lactate and ^{13}C-bicarbonate metabolism in the human brain (Brooks, 2018; Uthayakumar et al., 2023). This suggests that a more realistic model, which considers compartmentalization and the reverse reaction of lactate-to-pyruvate, may be needed to recapitulate the underlying neurometabolism and will be explored in future work.

Due to J_{CH}-coupling, the [2–^{13}C]lactate signal appears as a doublet with a coupling constant of 146 Hz (Marjańska et al., 2010). This peak splitting needs to be accounted for in the acquisition to avoid deleterious off-resonance artifacts and signal cancelation. As shown by Datta and Spielman (2021), one approach could be to simultaneously excite both peaks and acquire data at two different echoes separated with a spacing of $1/2J_{CH}$. Alternatively, in this work, data for the upfield and downfield lactate peaks were acquired sequentially using a narrowband SPSP RF pulse. The lactate distribution appeared similarly across images of downfield and upfield signals prior to summation as seen from high correlation and SSIM values, and artifacts arising from J_{CH}-coupled signals were not observed. The whole brain k_{PL} values obtained using the summed lactate signal are similar to those reported for [1–^{13}C]lactate in the healthy human brain, indicating that the peak splitting and T_1 differences can be properly accounted for in the kinetic model (Autry et al., 2020). The large chemical shift separation between [2–^{13}C]pyruvate and [2–^{13}C]lactate may also be relevant at lower fields where T_1 relaxation times are shorter.

5. Conclusions

This research project developed a new approach using a specialized HP ^{13}C MR RF pulse sequence for acquiring volumetric and dynamic EPI of HP [2–^{13}C]pyruvate metabolism to [5–^{13}C]glutamate and to [2–^{13}C] lactate probing glycolytic and oxidative metabolism simultaneously, and demonstrated feasibility and initial results in five normal volunteer studies. The strategy of separately exciting the two peaks of the lactate doublet was shown to be feasible for imaging this metabolite with signal splitting. In combination with a variable resolution approach, the HP metabolite signals were utilized for quantifying k_{PL} and k_{PG} throughout the brain of healthy volunteers providing new measures of cerebral energy metabolism in humans enabling transition from prior research in the rat brain (Park et al., 2013; Park et al., 2016).

This study quantified the metabolism of HP [2–^{13}C]pyruvate to [2–^{13}C]lactate and [5–^{13}C]glutamate throughout the healthy human brain for the first time. Measuring of spatial localizations of pyruvate-to-lactate and pyruvate-to-glutamate conversions signifies an important step to use HP [2–^{13}C]pyruvate to investigate cerebral energy metabolism and potentially characterize brain tumors with isocitrate dehydrogenase (IDH) mutations.

Supplementary Material

Refer to Web version on PubMed Central for supplementary material.

Acknowledgments

This research was supported by NIH grants P41EB0135898, U01EB026412, P01CA118816, R01CA262630, R01CA273028, and the UCSF NICO project.

Declaration of Competing Interest

The authors declare the following financial interests/personal relationships which may be considered as potential competing interests:

Yaewon Kim reports financial support was provided by NIH.

Data availability

Data will be made available on request.

References

Abeyakoon O, Latifoltojar A, Gong F, Papoutsaki MV, Chowdhury R, Glaser M, Jeraj H, Awais R, Holt C, Twyman F, Arstad E, Gadian DG, Atkinson D, Comment A, O'Callaghan J, Smith L, Beeston T, Clemente J, Patani N, Stein R, Yuneva M, Szabadkai G, Halligan S, Punwani S, 2019. Hyperpolarised ^{13}C MRI: a new horizon for non-invasive diagnosis of aggressive breast cancer. BJR Case Rep. 5 (3), 20190026 10.1259/bjrcr.20190026. [PubMed: 31555479]

Aggarwal R, Vigneron DB, Kurhanewicz J, 2017. Hyperpolarized 1- [^{13}C]-pyruvate magnetic resonance imaging detects an early metabolic response to androgen ablation therapy in prostate cancer. Eur. Urol 72 (6), 1028–1029. 10.1016/j.eururo.2017.07.022. [PubMed: 28765011]

Ardenkjaer-Larsen JH, Fridlund B, Gram A, et al. , 2003. Increase in signal-to-noise ratio of >10,000 times in liquid-state NMR. Proc. Natl. Acad. Sci. U. S. A 100 (18), 10158–10163. 10.1073/pnas.1733835100. [PubMed: 12930897]

Autry AW, Gordon JW, Carvajal L, Mareyam A, Chen HY, Park I, Mammoli D, Vareth M, Chang SM, Wald LL, Xu D, Vigneron DB, Nelson SJ, Li Y, 2019. Comparison between 8- and 32-channel phased-array receive coils for *in vivo* hyperpolarized ^{13}C imaging of the human brain. Magn. Reson. Med 82 (2), 833–841. 10.1002/mrm.27743. [PubMed: 30927300]

Autry AW, Gordon JW, Chen HY, LaFontaine M, Bok R, Van Criekinge M, Slater JB, Carvajal L, Villanueva-Meyer JE, Chang SM, Clarke JL, Lupo JM, Xu D, Larson PEZ, Vigneron DB, Li Y, 2020. Characterization of serial hyperpolarized ^{13}C metabolic imaging in patients with glioma. Neuroimage Clin 27, 102323 10.1016/j.nicl.2020.102323. [PubMed: 32623139]

Autry AW, Lafontaine M, Jalbert L, Phillips E, Phillips JJ, Villanueva-Meyer J, Berger MS, Chang SM, Li Y, 2022. Spectroscopic imaging of D-2-hydroxyglutarate and other metabolites in pre-surgical patients with IDH-mutant lower-grade gliomas. J. Neurooncol 159 (1), 43–52. 10.1007/s11060-022-04042-3. [PubMed: 35672531]

Autry AW, Park I, Kline C, Chen HY, Gordon JW, Raber S, Hoffman C, Kim Y, Okamoto K, Vigneron DB, Lupo JM, Prados M, Li Y, Xu D, Mueller S, 2021. Pilot study of hyperpolarized ^{13}C metabolic

imaging in pediatric patients with diffuse intrinsic pontine glioma and other CNS cancers. Am. J. Neuroradiol 42 (1), 178–184. 10.3174/ajnr.A6937. [PubMed: 33272950]

Bogner W, Gruber S, Trattnig S, Chmelik M, 2012. High-resolution mapping of human brain metabolites by free induction decay (1)H MRSI at 7 T, 1H FID MRSI IN THE human brain AT 7 T. NMR Biomed 25 (6), 873–882. 10.1002/nbm.1805. [PubMed: 22190245]

Brooks GA, 2018. The science and translation of lactate shuttle theory. Cell Metab 27 (4), 757–785. 10.1016/j.cmet.2018.03.008. [PubMed: 29617642]

Chaumeil MM, Larson PE, Woods SM, Cai L, Eriksson P, Robinson AE, Lupo JM, Vigneron DB, Nelson SJ, Pieper RO, Phillips JJ, Ronen SM, 2014. Hyperpolarized [1-^{13}C] glutamate: a metabolic imaging biomarker of IDH1 mutational status in glioma. Cancer Res 15 (16), 4247–4257. 10.1158/0008-5472.CAN-14-0680, 74.

Chen J, Patel TR, Pinho MC, Choi C, Harrison CE, Baxter JD, Derner K, Pena S, Liticker J, Raza J, Hall RG, Reed GD, Cai C, Hatanpaa KJ, Bankson JA, Bachoo RM, Malloy CR, Mickey BE, Park JM, 2021. Preoperative imaging of glioblastoma patients using hyperpolarized ^{13}C pyruvate: potential role in clinical decision making. Neurooncol. Adv 28 (1), vdab092. 10.1093/noajnl/vdab092, 3.

Chung BT, Chen HY, Gordon J, Mammoli D, Sriram R, Autry AW, Le Page LM, Chaumeil MM, Shin P, Slater J, Tan CT, Suszczynski C, Chang S, Li Y, Bok RA, Ronen SM, Larson PEZ, Kurhanewicz J, Vigneron DB, 2019. First hyperpolarized [2-^{13}C]pyruvate MR studies of human brain metabolism. J. Magn. Reson 309, 106617 10.1016/j.jmr.2019.106617. [PubMed: 31648132]

Cunningham CH, Lau JY, Chen AP, Geraghty BJ, Perks WJ, Roifman I, Wright GA, Connelly KA, 2016. Hyperpolarized ^{13}C metabolic MRI of the human heart: initial experience. Circ. Res 119 (11), 1177–1182. 10.1161/CIRCRESAHA.116.309769. [PubMed: 27635086]

Datta K, Spielman D, 2021. MRI of [2-^{13}C]lactate without J-coupling artifacts. Magn. Reson. Med 85 (3), 1522–1539. 10.1002/mrm.28532. [PubMed: 33058240]

Dominguez-Viqueira W, Geraghty BJ, Lau JYC, Robb FJ, Chen AP, Cunningham CH, 2016. Intensity correction for multichannel hyperpolarized ^{13}C imaging of the heart. Magn. Reson. Med 75 (2), 859–865. 10.1002/mrm.26042. [PubMed: 26619820]

Gallagher FA, Woitek R, McLean MA, Gill AB, Manzano Garcia R, Provenzano E, Riemer F, Kaggie J, Chhabra A, Ursprung S, Grist JT, Daniels CJ, Zaccagna F, Laurent MC, Locke M, Hilborne S, Frary A, Torheim T, Boursnell C, Schiller A, Patterson I, Slough R, Carmo B, Kane J, Biggs H, Harrison E, Deen SS, Patterson A, Lanz T, Kingsbury Z, Ross M, Basu B, Baird R, Lomas DJ, Sala E, Wason J, Rueda OM, Chin SF, Wilkinson IB, Graves MJ, Abraham JE, Gilbert FJ, Caldas C, Brindle KM, 2020. Imaging breast cancer using hyperpolarized carbon-13 MRI. Proc. Natl. Acad. Sci. U. S. A 117 (4), 2092–2098. 10.1073/pnas.1913841117. [PubMed: 31964840]

Golman K, Ardenkjaer-Larsen JH, Petersson JS, Mansson S, Leunbach I, 2003. Molecular imaging with endogenous substances. Proc. Natl. Acad. Sci. U. S. A 100 (18), 10435–91043. 10.1073/pnas.1733836100. [PubMed: 12930896]

Golman K, Zandt RI, Lerche M, Pehrson R, Ardenkjaer-Larsen JH, 2006. Metabolic imaging by hyperpolarized ^{13}C magnetic resonance imaging for *in vivo* tumor diagnosis. Cancer Res 66 (22), 10855–10860. 10.1158/0008-5472.CAN-06-2564. [PubMed: 17108122]

Gordon JW, Autry AW, Tang S, Graham JY, Bok RA, Zhu X, Villanueva-Meyer JE, Li Y, Ohliger MA, Abraham MR, Xu D, Vigneron DB, Larson PEZ, 2020. A variable resolution approach for improved acquisition of hyperpolarized ^{13}C metabolic MRI. Magn. Reson. Med 84 (6), 2943–2952. 10.1002/mrm.28421. [PubMed: 32697867]

Granlund KL, Tee SS, Vargas HA, Lyashchenko SK, Reznik E, Fine S, Laudone V, Eastham JA, Touijer KA, Reuter VE, Gonen M, Sosa RE, Nicholson D, Guo YW, Chen AP, Tropp J, Robb F, Hricak H, Keshari KR, 2020. Hyperpolarized MRI of human prostate cancer reveals increased lactate with tumor grade driven by monocarboxylate transporter 1. Cell Metab 31 (1) 10.1016/j.cmet.2019.08.024, 105–114.e3. [PubMed: 31564440]

Grist JT, McLean MA, Riemer F, et al. , 2019a. Quantifying normal human brain metabolism using hyperpolarized [1–13C]pyruvate and magnetic resonance imaging. Neuroimage 189, 171–179. 10.1016/j.neuroimage.2019.01.027. [PubMed: 30639333]

Grist JT, McLean MA, Riemer F, Schulte RF, Deen SS, Zaccagna F, Woitek R, Daniels CJ, Kaggie JD, Matys T, Patterson I, Slough R, Gill AB, Chhabra A, Eichenberger R, Laurent

MC, Comment A, Gillard JH, Coles AJ, Tyler DJ, Wilkinson I, Basu B, Lomas DJ, Graves MJ, Brindle KM, Gallagher FA, 2019b. Quantifying normal human brain metabolism using hyperpolarized [1-^{13}C] pyruvate and magnetic resonance imaging. Neuroimage 189, 171–179. 10.1016/j.neuroimage.2019.01.027. [PubMed: 30639333]

Hackett EP, Pinho MC, Harrison CE, Reed GD, Liticker Jeff, Raza J, Hall RG, Malloy CR, Barshikar S, Madden CJ, Park JM, 2020. Imaging acute metabolic changes in mild traumatic brain injury patients using hyperpolarized [1-^{13}C] pyruvate. iScience 23 (12), 101885. 10.1016/j.isci.2020.101885. [PubMed: 33344923]

Hangel G, Spurny-Dworak B, Lazen P, et al. , 2021. Inter-subject stability and regional concentration estimates of 3D-FID-MRSI in the human brain at 7 T. NMR Biomed 34 (12) 10.1002/nbm.4596.

Hoerst M, Weber-Fahr W, Tunc-Skarka N, et al. , 2010. Correlation of glutamate levels in the anterior cingulate cortex with self-reported impulsivity in patients with borderline personality disorder and healthy controls. Arch. Gen. Psychiatry 67 (9), 946–954. 10.1001/archgenpsychiatry.2010.93. [PubMed: 20603446]

Jenkinson M, Smith S, 2001. A global optimisation method for robust affine registration of brain images. Med. Image Anal 5, 143–156. 10.1016/S1361-8415(01)00036-6. [PubMed: 11516708]

Keshari KR, Wilson DM, 2014. Chemistry and biochemistry of ^{13}C hyperpolarized magnetic resonance using dynamic nuclear polarization. Chem. Soc. Rev 43 (5), 1627–1659. 10.1039/C3CS60124B. [PubMed: 24363044]

Kim Y, Chen HY, Autry AW, Villanueva-Meyer J, Chang SM, Li Y, Larson PEZ, Brender JR, Krishna MC, Xu D, Vigneron DB, Gordon JW, 2021. Denoising of hyperpolarized ^{13}C MR images of the human brain using patcsh-based higher-order singular value decomposition. Magn. Reson. Med 86 (5), 2497–2511. 10.1002/mrm.28887. [PubMed: 34173268]

Kurhanewicz J, Vigneron D, Bankson J, Brindle K, Cunningham C, Gallagher F, Keshari K, Kjaer A, Laustsen C, Mankoff D, Merritt M, Nelson S, Pauly J, Lee P, Ronen S, Tyler D, Rajan S, Spielman D, Wald L, Zhang X, Malloy C, Rizi R, 2019. Hyperpolarized ^{13}C MRI: path to clinical translation in oncology. Neoplasia 21 (1), 1–16. 10.1016/j.neo.2018.09.006. [PubMed: 30472500]

Larson PEZ, Chen HY, Gordon JW, et al. , 2018. Investigation of analysis methods for hyperpolarized ^{13}C-pyruvate metabolic MRI in prostate cancer patients: hyperpolarized pyruvate prostate cancer analysis methods. NMR Biomed 31 (11), e3997. 10.1002/nbm.3997. [PubMed: 30230646]

Lee CY, Soliman H, Geraghty BJ, et al. , 2020. Lactate topography of the human brain using hyperpolarized 13C-MRI. Neuroimage 204, 116202. 10.1016/j.neuroimage.2019.116202. [PubMed: 31557546]

Li Y, Vigneron DB, Xu D, 2021. Current human brain applications and challenges of dynamic hyperpolarized carbon-13 labeled pyruvate MR metabolic imaging. Eur. J. Nucl. Med. Mol. Imaging 48 (13), 4225–4235. 10.1007/s00259-021-05508-8. [PubMed: 34432118]

Lu J, Wang Z, Bier E, Leewiwatwong S, Mummy D, Driehuys B, 2022. Bias field correction in hyperpolarized ^{129}Xe ventilation MRI using templates derived by RF-depolarization mapping. Magn. Reson. Med 88 (2), 802–816. 10.1002/mrm.29254. [PubMed: 35506520]

Mammoli D, Carvajal L, Slater JB, et al. , 2020. Kinetic modeling of hyperpolarized carbon-13 pyruvate metabolism in the human brain. IEEE Trans. Med. Imaging 39 (2), 320–327. 10.1109/TMI.2019.2926437. [PubMed: 31283497]

Marjańska M, Iltis I, Shestov AA, Deelchand DK, Nelson C, Uğurbil K, Henry PG, 2010. *In vivo* ^{13}C spectroscopy in the rat brain using hyperpolarized [1-(13)C] pyruvate and [2-(13)C]pyruvate. J. Magn. Reson 206 (2), 210–218. 10.1016/j.jmr.2010.07.006. [PubMed: 20685141]

Miloushev VZ, Granlund KL, Boltyanskiy R, Lyashchenko SK, DeAngelis LM, Mellinghoff IK, Brennan CW, Tabar V, Yang TJ, Holodny AI, Sosa RE, Guo YW, Chen AP, Tropp J, Robb F, Keshari KR, 2018. Metabolic imaging of the human brain with hyperpolarized ^{13}C pyruvate demonstrates ^{13}C lactate production in brain tumor patients. Cancer Res 78 (14), 3755–3760. 10.1158/0008-5472.CAN-18-0221. [PubMed: 29769199]

Nelson SJ, Kurhanewicz J, Vigneron DB, Larson PE, Harzstark AL, Ferrone M, van Criekinge M, Chang JW, Bok R, Park I, Reed G, Carvajal L, Small EJ, Munster P, Weinberg VK, Ardenkjaer-Larsen JH, Chen AP, Hurd RE, Odegardstuen LI, Robb FJ, Tropp J, Murray JA, 2013. Metabolic imaging of patients with prostate cancer using hyperpolarized [1-^{13}C]pyruvate. Sci. Transl. Med 5 (198), 198ra08. 10.1126/scitranslmed.3006070.

Park I, Larson PEZ, Gordon JW, et al. , 2018a. Development of methods and feasibility of using hyperpolarized carbon-13 imaging data for evaluating brain metabolism in patient studies: hyperpolarized Carbon-13 Metabolic Imaging of Patients With Brain Tumors. Magn. Reson. Med 80 (3), 864–873. 10.1002/mrm.27077. [PubMed: 29322616]

Park I, Larson PEZ, Gordon JW, Carvajal L, Chen HY, Bok R, Van Criekinge M, Ferrone M, Slater JB, Xu D, Kurhanewicz J, Vigneron DB, Chang S, Nelson SJ, 2018b. Development of methods and feasibility of using hyperpolarized carbon-13 imaging data for evaluating brain metabolism in patient studies. Magn. Reson. Med 80 (3), 864–873. 10.1002/mrm.27077. [PubMed: 29322616]

Park JM, Josan S, Grafendorfer T, Yen YF, Hurd RE, Spielman DM, Mayer D, 2013. Measuring mitochondrial metabolism in rat brain *in vivo* using MR Spectroscopy of hyperpolarized [2-^{13}C]pyruvate. NMR Biomed 26 (10), 1197–1203. 10.1002/nbm.2935. [PubMed: 23553852]

Park JM, Josan S, Jang T, Merchant M, Watkins R, Hurd RE, Recht LD, Mayer D, Spielman DM, 2016. Volumetric spiral chemical shift imaging of hyperpolarized [2-(13)C]pyruvate in a rat c6 glioma model. Magn. Reson. Med 75 (3), 973–984. 10.1002/mrm.25766. [PubMed: 25946547]

Petroff OA, 2002. GABA and glutamate in the human brain. Neuroscientist 8 (6), 562–573. 10.1177/1073858402238515. [PubMed: 12467378]

Sanchez-Heredia JD, Olin RB, Grist JT, et al. , 2022. RF coil design for accurate parallel imaging on ^{13}C MRSI using ^{23}Na sensitivity profiles. Magn. Reson. Med 88 (3), 1391–1405. 10.1002/mrm.29259. [PubMed: 35635156]

Segovia G, Porras A, Del Arco A, Mora F, 2001. Glutamatergic neurotransmission in aging: a critical perspective. Mech. Ageing Dev 122 (1), 1–29. 10.1016/s0047-6374(00)00225-6. [PubMed: 11163621]

Stødkilde-Jørgensen H, Laustsen C, Hansen ESS, Schulte R, Ardenkjaer-Larsen JH, Comment A, Frøkiaer J, Ringgaard S, Bertelsen LB, Ladekarl M, Weber B, 2020. Pilot study experiences with hyperpolarized [1-(13)C]pyruvate MRI in pancreatic cancer patients. J. Magn. Reson. Imaging 51 (3), 961–963. 10.1002/jmri.26888. [PubMed: 31368215]

Sun C, Walker CM, Michel KA, Venkatesan AM, Lai SY, Bankson JA, 2018. Influence of parameter accuracy on pharmacokinetic analysis of hyperpolarized pyruvate: pharmacokinetic analysis of hyperpolarized pyruvate. Magn. Reson. Med 79 (6), 3239–3248. 10.1002/mrm.26992. [PubMed: 29090487]

Tran M, Latifoltojar A, Neves JB, Papoutsaki MV, Gong F, Comment A, Costa ASH, Glaser M, Tran-Dang MA, El Sheikh S, Piga W, Bainbridge A, Barnes A, Young T, Jeraj H, Awais R, Adeleke S, Holt C, O'Callaghan J, Twyman F, Atkinson D, Frezza C, Årstad E, Gadian D, Emberton M, Punwani S, 2019. First-in-human *in vivo* non-invasive assessment of intra-tumoral metabolic heterogeneity in renal cell carcinoma. BJR Case Rep 5 (3), 20190003 10.1259/bjrcr.20190003. [PubMed: 31428445]

Uthayakumar B, Soliman H, Chen AP, Bragagnolo N, Endre R, Perks WJ, Ma N, Heyn C, Cunningham CH, 2023. Evidence of lactate shuttling in the human brain using hyperpolarized^{13}C-MRI. BioRxiv [Preprint]. 10.1101/2023.01.13.523957.

Vaziri S, Autry AW, Lafontaine M, Kim Y, Gordon JW, Chen HY, Hu JY, Lupo JM, Chang SM, Clarke JL, Villanueva-Meyer JE, Bush NAO, Xu D, Larson PEZ, Vigneron DB, Li Y, 2022. Assessment of higher-order singular value decomposition denoising methods on dynamic hyperpolarized [1-^{13}C] pyruvate MRI data from patients with glioma. Neuroimage Clin 36, 103155 10.1016/j.nicl.2022.103155. [PubMed: 36007439]

Zhang Y, Brady M, Smith S, 2001. Segmentation of brain MR images through a hidden Markov random field model and the expectation-maximization algorithm. IEEE Trans. Med. Imaging 20, 45–57. 10.1109/42.906424. [PubMed: 11293691]

Zhou W, Bovik AC, Sheikh HR, Simoncelli EP, 2004. Image quality assessment: from error visibility to structural similarity. IEEE Trans. Image Process 13 (4), 600–612. 10.1109/TIP.2003.819861. [PubMed: 15376593]

Zhu Z, Zhu X, Ohliger MA, Tang S, Cao P, Carvajal L, Autry AW, Li Y, Kurhanewicz J, Chang S, Aggarwal R, Munster P, Xu D, Larson PEZ, Vigneron DB, Gordon JW, 2019. Coil combination methods for multi-channel hyperpolarized ^{13}C imaging data from human studies. J. Magn. Reson 301, 73–79. 10.1016/j.jmr.2019.01.01. [PubMed: 30851668]

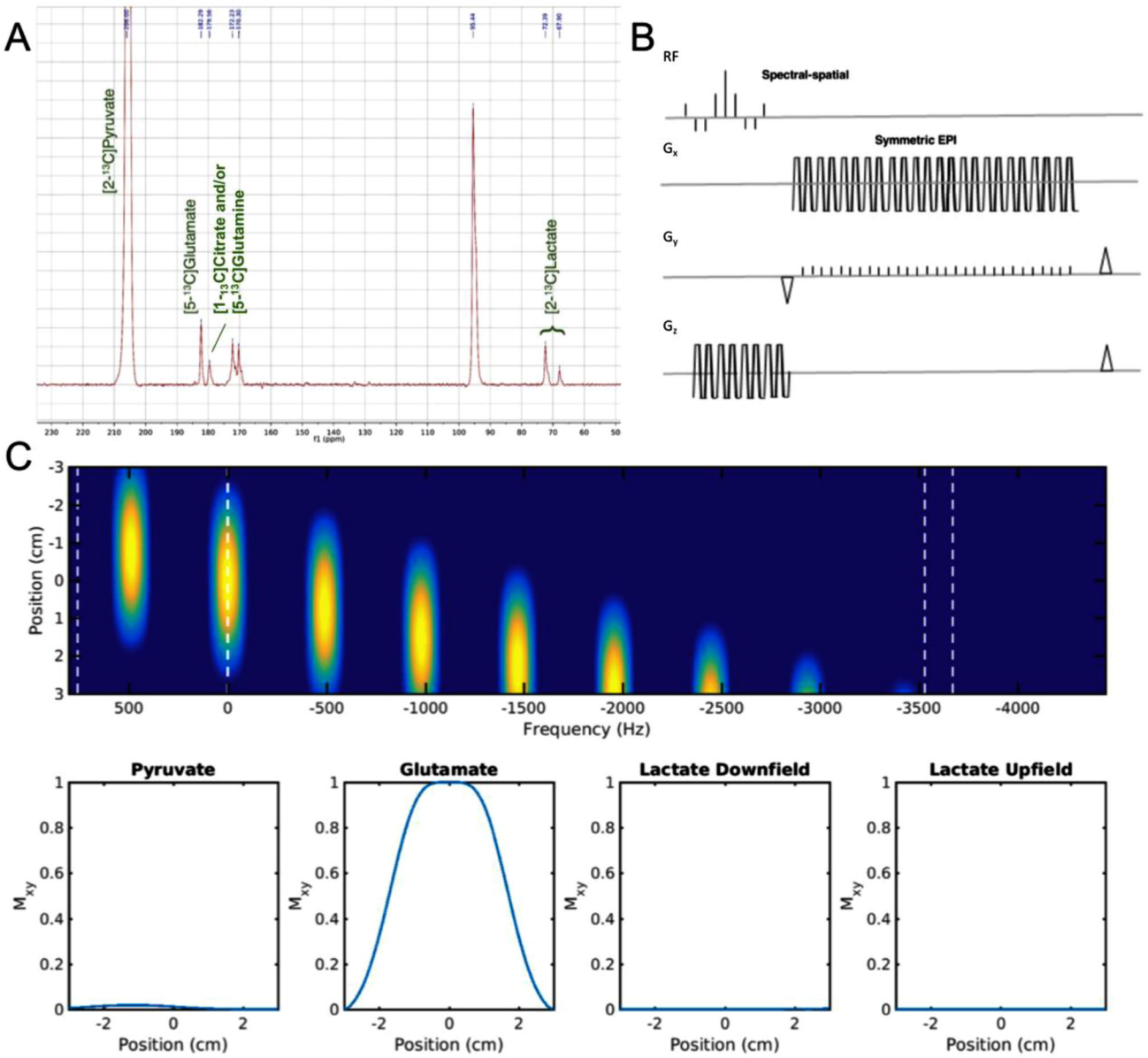

Fig. 1.

Singleband spectral-spatial RF pulse and EPI readout showing simulated responses from [2–^{13}C]pyruvate, [5–^{13}C]glutamate and [2–^{13}C]lactate to demonstrate the effectiveness of designed pass & stopbands. A. Chemical shift frequencies of [2–^{13}C]pyruvate and downstream metabolites were obtained from an NMR spectrum acquired in a previous study (Chung et al., 2019). The asymmetry of the lactate doublet is primarily due to the RF excitation band used. B. Sequence diagram illustrating the metabolite-selective EPI acquisition. C. The spectral-spatial response of the 2D RF pulse used to selectively excite [2–^{13}C]pyruvate (206.00 ppm), [5–^{13}C]glutamate (182.29 ppm), and the [2–^{13}C]lactate doublet (72.39 ppm and 67.90 ppm) with minimal off-resonance excitation. The vertical dashed lines correspond to the relative frequency for each metabolite at 3T. See

Supplementary Fig. 1 for frequency responses of the spectral-spatial RF pulse when centered on other resonances.

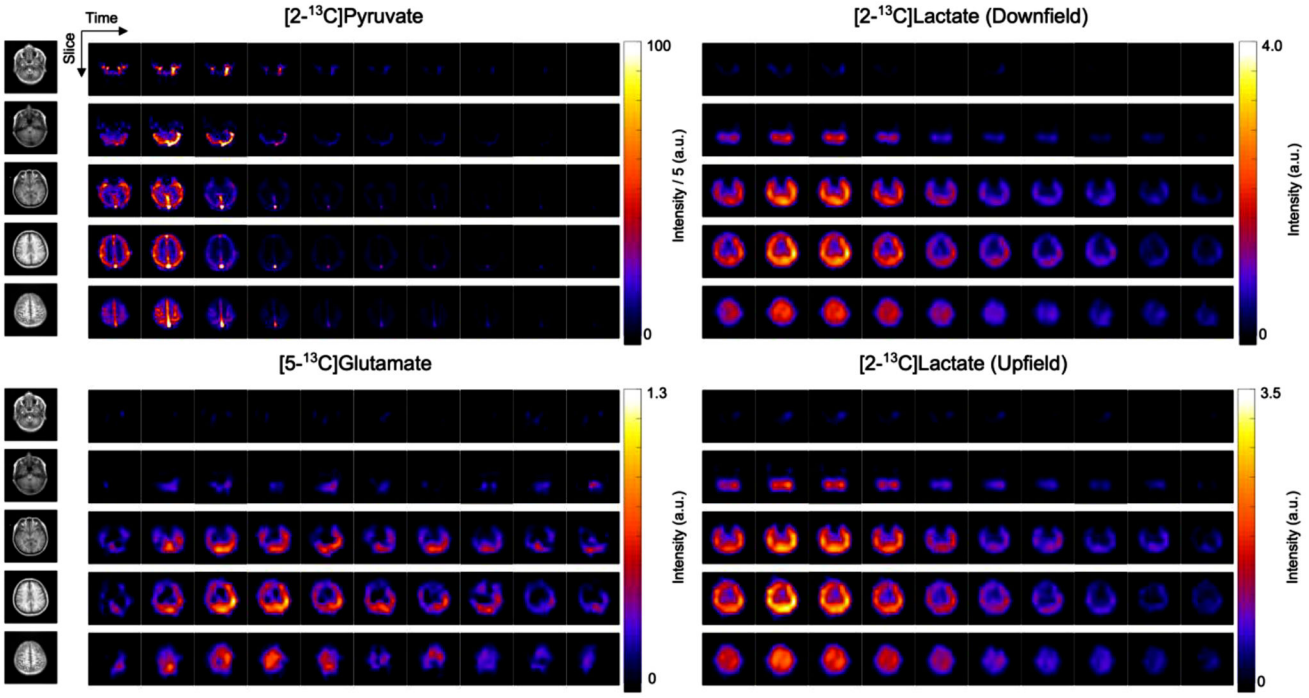

Fig. 2.

4D dynamics of HP [2–^{13}C]pyruvate, [5–^{13}C]glutamate, [2–^{13}C]lactate (downfield peak) and [2–^{13}C]lactate (upfield peak) from the human brain of a healthy volunteer (Vol-1). Displayed images show the first 10 timeframes with 3 second temporal resolution for a total of window of 30 s following denoising using a patch-based HOSVD method (Kim et al., 2021). Shown on the left are ^{1}H IR-SPGR anatomy images capturing average of slices. Upper window levels for [2–^{13}C]pyruvate data were adjusted to 20% of the maximum intensity. The images were denoised and zero-filled two-fold for display.

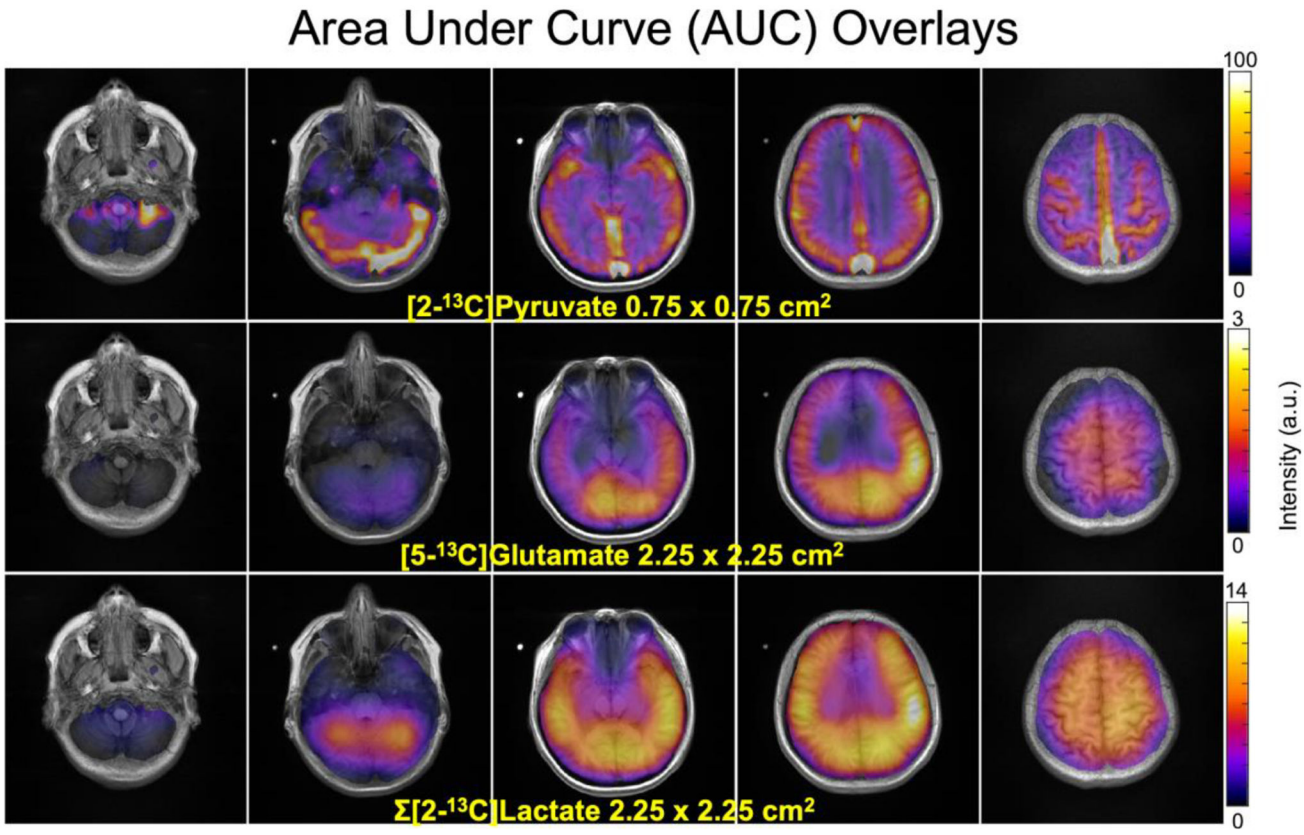

Fig. 3.

AUC (Area-Under-Curve) images from the volunteer (Vol-1) summed over 20 timeframes overlaid on ^{1}H IR-SPGR images. [2–^{13}C]lactate images illustrate acquired signal after summing both downfield and upfield peaks. High resolution (0.75 × 0.75 cm^{2}) pyruvate data shows strong arterial and venous signal, and a brain mask to reduce the pyruvate signal from adjacent muscle was consequently applied. The images were denoised and zero-filled for display.

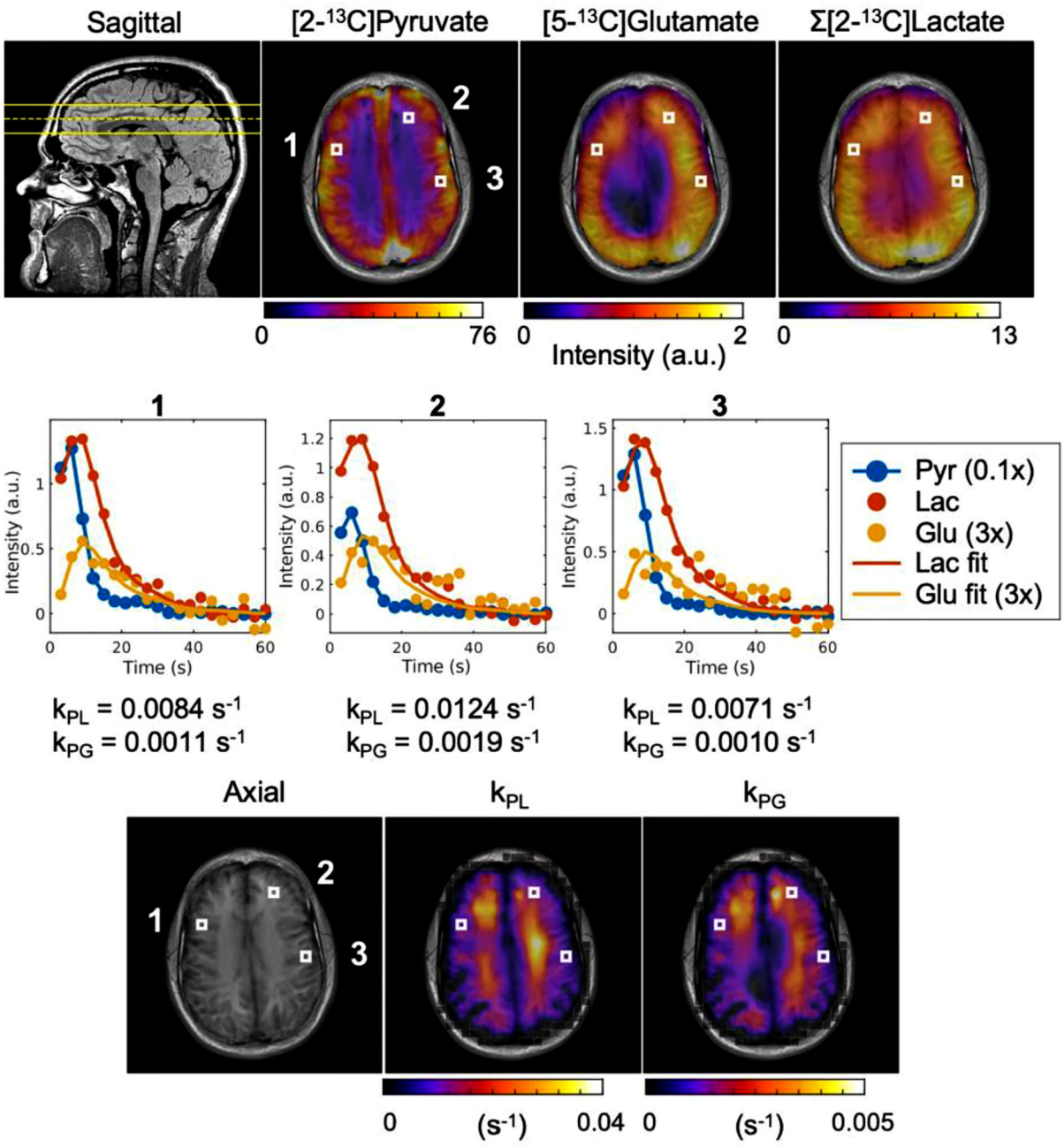

Fig. 4.

Kinetic analyses of dynamic HP [2–^{13}C]pyruvate data. (Top row) A sagittal ^{1}H FLAIR image from another volunteer showing a mid-slice position for ^{13}C EPI data denoted with yellow lines (dashed/solid: center/edge of the slice) and denoised ^{13}C AUC images for pyruvate, glutamate, and lactate overlaid on a corresponding axial ^{1}H SPGR image. (Middle row) Signal intensities of pyruvate, glutamate, and lactate over time from the selected voxels indicated in the AUC images. Kinetic fits for lactate and glutamate are displayed. (Bottom

row) Calculated k_{PL} and k_{PG} maps overlaid on axial ^{1}H SPGR image were obtained from healthy volunteer brain data. The selected voxels are also indicated in the k_{PL} and k_{PG} maps.